

Effective Field Theory and Scalar Triplet Dark Matter

Carolina Arbeláez^a, Marcela González^b, Martin Hirsch^c, Nicolás A. Neill^d,
Diego Restrepo^e

^a Universidad Técnica Federico Santa María and Centro Científico Tecnológico de Valparaíso CCTVal, Casilla 110-V, Valparaíso, Chile

^b Instituto de Física y Astronomía,
Universidad de Valparaíso,
Avenida Gran Bretaña 1111, Valparaíso, Chile

^cInstituto de Física Corpuscular (CSIC-Universitat de València),
C/ Catedrático José Beltrán 2, E-46980 Paterna (València), Spain

^d Departamento de Ingeniería Eléctrica-Electrónica,
Universidad de Tarapacá, Arica, Chile

^e Instituto de Física,
Universidad de Antioquia, Calle 70 No 52-21, Medellín, Colombia

carolina.arbelaez@usm.cl, marcela.gonzalezpi@uv.cl, mahirsch@ific.uv.es,
naneill@outlook.com, restrepo@udea.edu.co

Abstract

We discuss an extension of the standard model with a real scalar triplet, T , including non-renormalizable operators (NROs) up to $d = 6$. If T is odd under a Z_2 symmetry, the neutral component of T is a good candidate for the dark matter (DM) of the universe. We calculate the relic density and constraints from direct and indirect detection on such a setup, concentrating on the differences with respect to the simple model for a DM T with only renormalizable interactions. Bosonic operators can change the relic density of the triplet drastically, opening up new parameter space for the model. Indirect detection constraints, on the other hand, rule out an interesting part of the allowed parameter space already today and future CTA data will, very likely, provide a decisive test for this setup.

1 Introduction

Among the long list of proposed explanations for the dark matter (DM) in the universe, weakly interacting massive particles (WIMPs), are probably the solution which has been studied most. For reviews on WIMPs see, for example [1–3]. WIMPs are attractive candidates for a variety of reasons, not least among them the fact that their thermal production in the early universe makes it possible – in principle – to calculate definite predictions for cross sections for experiments searching for signals of DM today.

Any DM candidate must be able to reproduce the relic density (RD) as inferred from PLANCK data [4] and also obey a number of search constraints. For WIMPs, the most important bounds are those from two types of searches. First, there are the direct detection (DD) experiments, like LUX-ZEPLIN (LZ) [5, 6], and XENON-nt [7]. Future DD experiments, such as DARWIN [8], XLZD [9, 10] or also PandX-xt [11] will improve existing limits by (1-2) orders of magnitude. These constraints limit the list of possible WIMP candidates already today to a finite number of candidates [12, 13], and may exclude many more DM candidates (or discover the correct one!) in the future. Second, also indirect detection (ID) constraints¹ can be important. Existing data from H.E.S.S collaboration for 546 h [16, 17] already rule out interesting portions of parameter space, while the future CTA data [18, 19] is expected to lead to much stronger constraints.

The neutral component of a scalar triplet with hypercharge zero, T , can be a good WIMP dark matter candidate [20, 21]. A real T couples at the renormalizable level only to the standard model (SM) Higgs and this simple setup is quite predictive, since the relic DM density and the direct detection cross section essentially depend only on two parameters: The mass of T^0 and the quartic coupling of T to the SM Higgs. This minimal, renormalizable setup is, however, nowadays on the verge of being excluded by H.E.S.S data [16, 17] and will definitely be either discovered (or excluded) in the not-too-distant future, see the discussion in section 5.

However, in many models beyond the SM (BSM), the dark matter candidate is just the lightest particle of a possibly much more complicated “dark sector”.² These heavier dark sector particles can have important effects on the DM properties. For example, the relic density can change due to co-annihilation diagrams or s -channel resonances. One example diagram for each is shown for a toy model in fig. (1). Here, T is assumed to be the lightest Z_2 odd particle. On the left, we assume there is a second, heavier Higgs doublet, $S_{1,2,1/2}$, also odd under Z_2 .³ On the right, we added a $Z' = V_{1,1,0}$. This could be the vector of an extended gauge group, broken in the ultra-violet in such a way that a global Z_2 remains. Such an ansatz could explain the origin of the Z_2 , otherwise introduced by hand.

On the other hand, both toy models generate the same effective dimension six ($d = 6$) operator, $\mathcal{O}_3 \propto (H^\dagger D_\mu H)(TD^\mu T)$ in the limit where the scalar or vector mass are larger than m_T . In the case there is some hierarchy in the masses of the dark sector, effective field theories

¹For a recent discussion see for example [14, 15].

²The best known example for such a case is supersymmetry: In the MSSM (“minimal supersymmetric standard model”) all particles of the SM have a superpartner, odd under R-parity, the DM is just the lightest particle in the SUSY spectrum.

³If $S_{1,2,1/2}$ is the lightest odd particle, it can itself be the dark matter, the well-known inert doublet model (IDM) [22].

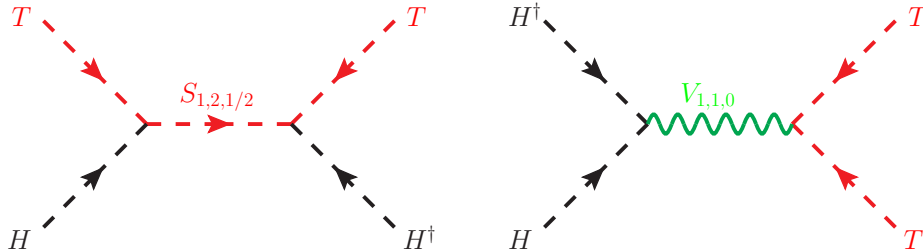


Figure 1: Co-annihilation diagram (left) for a model with dark matter triplet and an additional heavy (inert) scalar, $S_{1,2,1/2}$. This scalar is Z_2 odd. s-channel annihilation of the dark matter triplet (right) in a model with an additional vector, $Z' = V_{1,1,0}$. This vector is Z_2 even. In this setup the Z_2 could be a remnant of the symmetry breaking that gave the Z' its mass.

are therefore a useful tool for model-independent studies of dark matter phenomenology.

Indeed, application of EFTs for dark matter calculations has already gained some momentum in the past few years. For example, [23, 24] studied WIMP direct detection using low-energy EFT. Recently, [25] has given the complete set of operators up to dimension six ($d = 6$) for the case of models in which one dark matter particle (either scalar, fermion or vector) is added to the SM particle content. The paper [25] then studies in detail the dark matter phenomenology for a singlet scalar DM, $S_{1,1,0}$, and for heavy neutral lepton DM, $L' = F_{1,2,1/2}$. [26] used a sterile neutrino portal for a fermionic singlet DM, including non-renormalizable operators (NROs). Ref [27] adds singlets (either scalars, fermions or vectors) with NRO up to $d = 6$, and discusses how models with two dark vectors can explain dark matter via freeze-in. And there is the work of [28] which adds up to two DM particles and writes down the low-energy EFT operators up to $d = 7$. The authors call this “DSEFT”, dark sector effective field theory.

In our current work, we will study the phenomenology of a dark matter T adding NROs. We will call this framework TSMEFT, i.e. the “standard model effective field theory supplemented by a scalar triplet”. In the next section, we will briefly introduce the model lagrangian. Section 3 discusses, how the different, possible $d = 6$ operators affect the relic density of the dark matter candidate. In section 4 we discuss, how operators are constrained from direct and indirect detection experiments and discuss briefly, which data will be important for us. Section 5 then shows the main results of this paper. There, we will discuss our numerical results and show, which operators are most (and least) constrained at present for a DM model with a hyperchargeless triplet. We then close with a short summary and conclusion. For completeness, in appendix A.1 we list for also operators odd in T , while in A.2 we discuss possible, additional operators for a complex T . Finally, in appendix A.3 we list possible tree-level UV completions for the operators studied in this paper.

2 Scalar triplet lagrangian up to $d = 6$

We add a scalar $S_{1,3,0} = T$ to the SM particle content. We will consider the simpler case of T being real. The renormalizable Lagrangian of the model consists of the SM Lagrangian,

plus the following new terms:

$$\mathcal{L}^{\text{TSM}} = \mathcal{L}^{\text{SM}} + \frac{1}{2}m_T^2 T^2 + \mu_T(H^\dagger H)T + \text{h.c.} + \frac{1}{2}\lambda_{HT}H^\dagger HT^2 - \frac{1}{4}\lambda_T T^4. \quad (1)$$

The term proportional to μ_T allows the field T to decay to SM particles. We will forbid this term and all other terms odd in T by assuming a Z_2 symmetry under which the only odd particle is T .

Apart from the renormalizable lagrangian, eq. (1), we will add non-renormalizable operators up to dimension 6:

$$\mathcal{L} = \mathcal{L}^{\text{TSM}} + \sum_i \frac{C_i}{\Lambda^{d-4}} \mathcal{O}_i. \quad (2)$$

Table 1 lists all possible effective operators (up to $d = 6$), which contain an even number of T 's. We do not write the Wilson coefficients explicitly, for operators with standard model fermions the coefficients are matrices in flavour space. The table defines the operators, gives the number of free parameters in the Wilson coefficients and whether the operator is self-conjugate or not. For completeness, in appendix A.1 we also give operators odd in T up to $d = 6$.

Not all of the operators in table 1 will be important for dark matter phenomenology. Operators $\mathcal{O}_{11} - \mathcal{O}_{13}$ do not lead to any change in the number density of T in the early universe and we have therefore not included them in our numerical studies. Also, \mathcal{O}_{10} is a six-particle operator, sub-dominant to \mathcal{O}_3 in its effects on DM phenomenology. We do not study this operator in detail either.

Numerically, we only calculate the effects of NROs. However, one should keep in mind that there are special kinematic configurations, for which the use of EFTs is *not* well justified. The best example for this is probably the s-channel diagram on the right of fig. (1) in the special case where $m_T \simeq m_{Z'}/2$. In this case the cross section will be resonantly enhanced and this effect is not captured by the EFT. It may therefore be of interest in some cases to go to model-dependent studies. While this is beyond the scope of the present work, in appendix A.3, we give all possible tree-level completions for operators $\mathcal{O}_1 - \mathcal{O}_9$ for completeness. Recall, two example diagrams for toy UV models for \mathcal{O}_3 were already discussed briefly in the introduction.

3 Relic density

In this section we study the effects of the operators $\mathcal{O}_1 - \mathcal{O}_9$ on the DM relic abundance, Ωh^2 . The operators are listed in table 1. We have implemented all nine operators in `CalCHEP` format [29] using `FeynRules` [30] and calculated the relic density of DM numerically using `MicrOMEGAs` [31–33]. Results for all operators will be discussed in section 5.

However, let us first discuss some basics of DM freeze-out which will allow us to understand the numerical results qualitatively. The DM relic abundance Ωh^2 generated within the standard thermal WIMP paradigm depends of the thermal average of the DM annihilation cross section times the relative DM velocity, $\langle\sigma v\rangle$. It can be written as [34]:

$$\Omega h^2 = \frac{1.09 \times 10^9 \text{ GeV}^{-1}}{g_*^{1/2} m_{\text{Pl}}} \frac{1}{J(x_f)}, \quad J(x) = \int_x^\infty \frac{\langle\sigma v\rangle}{x^2} dx. \quad (3)$$

Name	Operator	# parameters	+h.c.?
\mathcal{O}_1	$(\bar{L}\gamma_\mu L)(TD^\mu T)$	9	no
\mathcal{O}_2	$(\bar{Q}\gamma_\mu Q)(TD^\mu T)$	9	no
\mathcal{O}_3	$(H^\dagger D_\mu H)(TD^\mu T)$	2	no
\mathcal{O}_4	$\bar{L}e_R H T T$	18	yes
\mathcal{O}_5	$\bar{Q}d_R H T T$	18	yes
\mathcal{O}_6	$\bar{Q}u_R H^\dagger T T$	18	yes
\mathcal{O}_7	$B^{\mu\nu} B_{\mu\nu} T T$	1	no
\mathcal{O}_8	$W^{\mu\nu} W_{\mu\nu} T T$	1	no
\mathcal{O}_9	$G^{\mu\nu} G_{\mu\nu} T T$	1	no
\mathcal{O}_{10}	$H^\dagger H^\dagger H H T T$	2	no
\mathcal{O}_{11}	$H^\dagger H T T T T$	1	no
\mathcal{O}_{12}	$(TD^\mu T)(TD_\mu T)$	1	no
\mathcal{O}_{13}	T^6	1	no

Table 1: Operators even in T in TSMEFT at $d = 6$. This set of operators is allowed for a T odd under Z_2 . Operators $\mathcal{O}_{10} - \mathcal{O}_{13}$ are listed only for completeness, they are less important for the phenomenology studied in this paper.

Here, $m_{\text{Pl}} = 1.22 \times 10^{19}$ GeV is the Planck mass, g_* denotes the total number of relativistic degrees of freedom at freeze-out⁴. $x_f = m_{T^0}/T_f$ is the usual ratio of the DM mass to the freeze-out temperature T_f and $J(x)$ represents the efficiency of the post freeze-out annihilation. In the non-relativistic limit, the thermal averaged cross section has a linear dependence with the temperature as $\langle\sigma v\rangle = a + 6b T/m_{T^0}$ (here T is the temperature), where a and b are terms describing the non-relativistic cross section Taylor expansion in v^2 as $\sigma \sim a + bv^2$ [34].

For the total annihilation cross section there will be two contributions in our case. First, there is the contribution from gauge interactions. This case has been calculated in [20], and for the case of a hypercharge zero electro-weak triplet, the result for the dominant annihilation channel to gauge bosons is simply:

$$\langle\sigma v\rangle = \frac{g_2^4}{4\pi m_{T^0}^2}. \quad (4)$$

This cross section has the typical $m_{T^0}^{-2}$ dependence for a thermal WIMP. Second, all nine operators, listed in table 1, contribute to the DM annihilation. The cross section associated

⁴In the SM, $g_* \sim 120$ at $T \sim 1$ TeV and $g_* \sim 65$ at $T \sim 1$ GeV.

to any $d = 6$ NRO can be written schematically as:

$$\sigma_i \sim \frac{C_i^2}{4\pi\Lambda^4} f_i(m_{T^0}, s, \dots), \quad (5)$$

where f_i represents a function, specific to each operator, that depends on kinematic variables, such as the DM mass and the center of mass energy, \sqrt{s} , and so on.

We have used CalcHEP [35], to calculate f_2 and f_3 (corresponding to \mathcal{O}_2 and \mathcal{O}_3 from table 1). The result is:

$$f_2 = a_2 m_q^2 \sqrt{\frac{(s - 4m_q^2)}{(s - 4m_{T^0}^2)}}, \quad f_3 = a_3 s \sqrt{\frac{(s - 4m_h^2)}{(s - 4m_{T^0}^2)}}, \quad (6)$$

where $a_{2,3}$ are dimensionless numerical factors. Since in the non-relativistic limit s is given approximately as $s \sim 4m_{T^0}^2(1 + v_{cm}^2)$, with v_{cm} the velocity of the DM particle, one can approximate the σ_i in the limit where $m_q, m_h \ll m_{T^0}$ roughly as being $\sigma_2 \propto m_q^2/\Lambda^4$ and $\sigma_3 \propto m_{T^0}^2/\Lambda^4$.

Let us first discuss the case of \mathcal{O}_3 , see fig. 2. The figure shows the calculated relic density, Ωh^2 , as function of the mass of the dark matter candidate, for the case $\lambda_{HT} = 0$ ⁵, for different choices of C_3 (left) and for fixed $C_3 = 1$ and different choices of Λ (right). The grey band indicates the allowed range of the DM density, as determined by PLANCK [4], at 3σ C.L.

One can understand the observed behaviour with the help of the equations given above. For smaller DM masses the calculated relic density rises with increasing masses. This rise continues for all values of m_{T^0} for the smallest Wilson coefficient shown, $C_3 = 0.1$ (on the left). Since $\Omega h^2 \propto 1/\sigma$, eq. (3), this behaviour directly reflects that for gauge interactions $\sigma \propto 1/m_{T^0}^2$, see eq. (4). For larger values of C_3 the relic density starts to decrease again for large values of m_{T^0} . This indicates the parameter region where $\sigma \propto m_{T^0}^2/\Lambda^4$, i.e. where the contribution from \mathcal{O}_3 becomes dominant.

The plot on the right of fig. 2 shows Ωh^2 as function of m_{T^0} for different choices of Λ , for $C_3 = 1$. The lines in this plot stop at $m_{T^0} \simeq \Lambda$, since we use EFT to calculate the annihilation cross section. In fact, a consistent EFT requires $m_{T^0} \ll \Lambda$, thus the calculation becomes less reliable, when m_{T^0} approaches Λ .⁶ For values of Λ larger than $\Lambda \sim 15$ TeV the contributions from the operator will become sub-dominant relative to the gauge interactions, unless we take C_3 larger than 1.

Fig. 3 shows the relic density versus m_{T^0} for the first nine operators listed in table 1. The plots contain a black line labeled ‘‘PG’’, for the case of pure gauge interactions (all operators switched off). In this figure, we show to the left (right) the calculation without (including) the Sommerfeld effect. In the calculation of the Sommerfeld effect, we follow the description outlined in ref. [21]. These plots fix $\Lambda = 15$ TeV and all C_i at their maximum value allowed by perturbativity $C_i = 4\pi$.

⁵We focus on the case $\lambda_{HT} = 0$ in order to highlight the contribution of the effective operators. For the effect of $\lambda_{HT} \neq 0$ in the pure gauge scenario, see ref. [36, 37].

⁶For UV models which generate the operator via t -channel diagrams, departure from EFT is expected to be of order $(m_{T^0}/\Lambda)^2$.

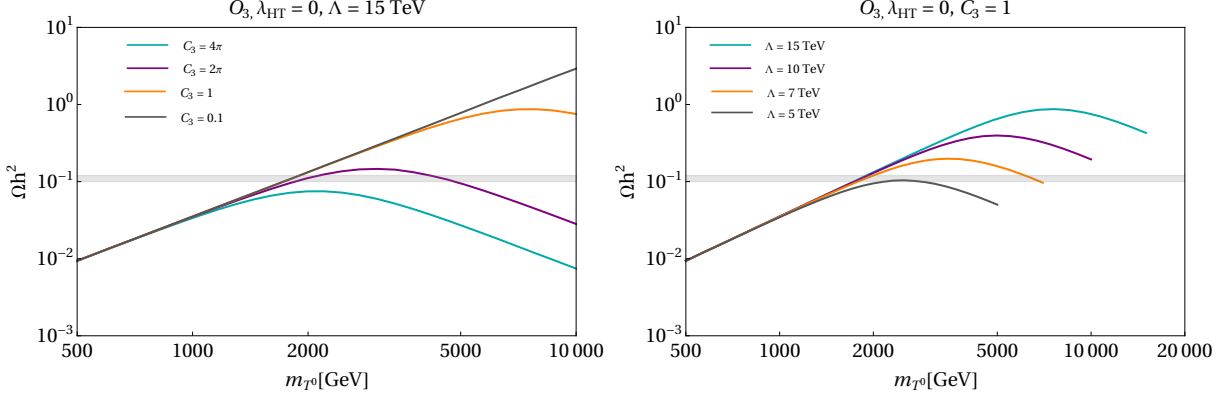


Figure 2: Relic density as a function of m_{T^0} (the mass of the dark matter candidate) with only C_3 , the Wilson coefficient of \mathcal{O}_3 , different from zero. To the left: For a fixed scale $\Lambda = 15$ TeV and different values of C_3 ; to the right: For fixed $C_3 = 1$ and different values of the scale Λ . For this figure, we fixed $\lambda_{HT} = 0$.

One can clearly distinguish two groups of curves. There are the operators $\mathcal{O}_{1,2,4,5,6}$ involving fermions and the operators involving bosons, $\mathcal{O}_{3,7,8,9}$. The different behaviour can be understood from eq. (6). Operators involving fermions in the final state are chirally suppressed, i.e. $\sigma \propto m_f^2$. These operators are therefore usually only a sub-dominant contribution in the total annihilation cross section, compared to the gauge interactions. Note that, operators involving fermions carry generation indices, i.e. $C_k \rightarrow (C_k)^{ij}$, with $i, j = 1, 2, 3$. For this figure we switched on the coefficients for all family indices, but due to $\sigma \propto m_{f_i}^2$ the 3rd generation indices completely dominate the calculation.

Bosonic operators, on the other hand, lead to cross sections $\sigma \propto m_{T^0}^2/\Lambda^4$. Thus, for $\mathcal{O}_{3,7,8,9}$ the relic density calculation will be completely dominated by the operator contribution at larger values of m_{T^0} . In section 5 we will therefore concentrate the discussion on the bosonic operators.

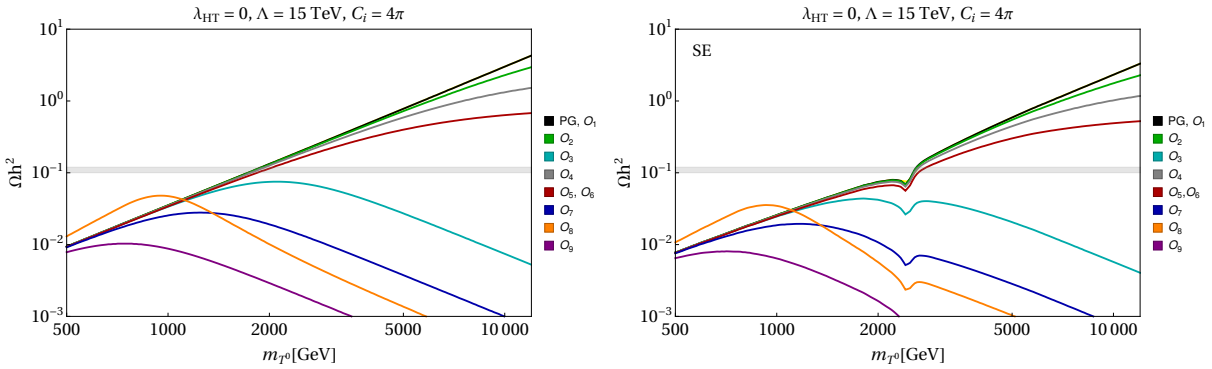


Figure 3: Top panel: Relic density as a function of m_{T^0} for the operators $\mathcal{O}_1 - \mathcal{O}_9$ in table 1, ignoring (left) and including (right) the Sommerfeld effect.

4 Constraints from Direct and Indirect Detection

In this section, we discuss the constraints from both direct and indirect detection experiments on the effective operators \mathcal{O}_{1-9} .

In the case of the direct detection, we derive the expression for the cross section analytically. The expression for the case of a scalar $SU(2)$ triplet (without NROs) can be found in Ref. [36]. Here we add the contribution of the different higher dimensional operators.

The spin-independent direct detection cross section for a DM particle T^0 scattering off a nucleus N is given by [38]

$$\sigma_{SI} = \frac{|\mathcal{M}_{fi}|^2}{16\pi(m_N + m_{T^0})^2}, \quad (7)$$

where m_N , m_{T^0} are the nucleus and dark matter particle masses, respectively, and \mathcal{M}_{fi} is the corresponding amplitude:

$$\mathcal{M}_{fi} = \langle NT^0 | \mathcal{L}_{\text{int}} | NT^0 \rangle. \quad (8)$$

The operators from our effective Lagrangian (see table 1) that contribute to this amplitude at the tree level are those involving quark currents (\mathcal{O}_5 and \mathcal{O}_6) and gluons (\mathcal{O}_9). Although \mathcal{O}_2 also involves quarks, its contribution is negligible as it is proportional to the square of the dark matter velocity (v_{DM}^2). The remaining operators, which do not involve quarks or gluons, are all negligible at the tree level. Using the following expressions for the matrix elements⁷ [31, 39, 40]:

$$\langle N | \frac{\alpha_S}{\pi} G_{\mu\nu}^a G^{a\mu\nu} | N \rangle = -\frac{8}{9} f_{TG}^N m_N, \quad f_{TG}^N = 1 - \sum_{q=u,d,s} f_{Tq}^N, \quad (9)$$

$$\langle N | m_q \bar{q}q | N \rangle = f_{Tq}^N m_N, \quad (10)$$

where $f_{Tu}^N = 0.0153(0.011)$, $f_{Td}^N = 0.0191(0.0273)$, $f_{Ts}^N = 0.0447(0.0447)$ for the proton (neutron) [31] and consequently $f_{TG}^N = 0.921(0.917)$, we find:

$$\left\langle NT^0 \left| \frac{C_5^{ij} \mathcal{O}_5^{ij}}{\Lambda^2} \right| NT^0 \right\rangle = \frac{C_5^{ij}}{\Lambda^2} \langle NT^0 | \bar{Q}_i d_{Rj} H T T | NT^0 \rangle = \frac{C_5^{ij}}{\Lambda^2} \frac{2v}{\sqrt{2}m_{d_i}} f_{d_i}^N \delta_{ij} 2m_N^2, \quad (11)$$

$$\left\langle NT^0 \left| \frac{C_6^{ij} \mathcal{O}_6^{ij}}{\Lambda^2} \right| NT^0 \right\rangle = \frac{C_6^{ij}}{\Lambda^2} \langle NT^0 | \bar{Q} u_R H^\dagger T T | NT^0 \rangle = \frac{C_6^{ij}}{\Lambda^2} \frac{2v}{\sqrt{2}m_{u_i}} f_{u_i}^N \delta_{ij} 2m_N^2, \quad (12)$$

$$\left\langle NT^0 \left| \frac{C_9 \mathcal{O}_9}{\Lambda^2} \right| NT^0 \right\rangle = \frac{C_9}{\Lambda^2} \langle NT^0 | G^{\mu\nu} G_{\mu\nu} T T | NT^0 \rangle = \frac{C_9}{\Lambda^2} \frac{4\pi}{\alpha_s} \left(-\frac{4}{9} f_{TG}^N 2m_N^2 \right), \quad (13)$$

⁷These expressions use the non-relativistic normalization for nucleon one-particle states, while eqs. (11)-(13) use relativistic normalization, i.e., we have introduced the corresponding replacements $|N\rangle \rightarrow \sqrt{2E_N} |N\rangle \approx \sqrt{2m_N} |N\rangle$ when writing eqs. (11)-(13).

Finally, the expression for the direct detection cross section including the effect of the effective operators is

$$\sigma_{\chi N} = \frac{\mu_{\chi N}^2 m_N^2}{4\pi m_\chi^2} \left[\frac{2\lambda_{\chi H}}{m_h^2} f^N + \frac{C_5^{11}}{\Lambda^2} \frac{2v}{\sqrt{2}m_d} f_{Td}^N + \frac{C_5^{22}}{\Lambda^2} \frac{2v}{\sqrt{2}m_s} f_{Ts}^N + \frac{C_6^{11}}{\Lambda^2} \frac{2v}{\sqrt{2}m_u} f_{Tu}^N + \right. \\ \left. - \left(f_2^g + \frac{4\pi C_9}{\alpha_s \Lambda^2} \right) \frac{4}{9} f_{TG}^N + \frac{3\pi\alpha_2^2}{4} \frac{m_\chi}{m_W^3} f_{PDF}^N \right]^2, \quad (14)$$

where $f^N = 0.287(0.284)$ and $f_{PDF}^N = 0.526(0.526)$ for proton (neutron) [36].

On the other hand, for the case of indirect detection bounds, we compute the gamma-ray flux arising from the annihilation of dark matter particles into gamma-rays, by using **MicrOMEGAs**. We will subsequently study the complementarity of these predictions with direct detection searches, emphasizing the potential for detecting gamma-ray signals from each operator within the effective Lagrangian.

In this way, we will obtain the excluded regions of the parameter space for each operator by comparing the gamma-ray flux with the observational data from the H.E.S.S collaboration, and also the corresponding CTA excluded prospects. In all of them an Einasto profile [41] for the DM halo is assumed. Large uncertainties are expected when other profiles are assumed, like the Navarro, Frenk and White (NFW) profile [42, 43]. Hence, the excluded and projected sensitivity regions in our results, could increase or decrease if other profiles for the dark matter halo are used. For the excluded regions in the W^+W^- , ZZ and $b\bar{b}$ channels we will use the data for 546 h from H.E.S.S [16], and the CTA prospects from [18]. While for $\gamma\gamma$, we use the data for 546 h from H.E.S.S [17] and the CTA prospects from [19]. Fermi-LAT bounds [44] are slightly weaker than H.E.S.S for the explored regions of the parameter space, and are not used at all in our analysis.

5 Numerical results

In this section we present our numerical results. We will study the impact of the effective operators, see table 1, considering one operator at a time. As discussed above, see sections 2 and 3, we can divide the operators in table 1 in three groups. First there are the operators that will be irrelevant for dark matter phenomenology, i.e. \mathcal{O}_{10-13} . The remaining operators we divide into (purely) bosonic operators, $\mathcal{O}_{3,7,8,9}$, and operators with fermions, $\mathcal{O}_{1,2,4,5,6}$. As shown in section 3, the latter affect the relic density only mildly, thus from the fermionic operators we will show only the results for one example operator, i.e. \mathcal{O}_6 .

In all cases discussed in this section, the relic abundance of dark matter and the indirect detection cross section calculation for each operator was performed using **MicrOMEGAs** [31–33], while the direct detection cross section was obtained using the analytically calculated cross sections given in section 4, see eq. (14). We use the limits on direct detection cross sections from LUX-ZEPLIN (LZ) experiment from ref. [6]. Limits from XENON-nt are similar, but currently slightly weaker [7]. The projected future bounds for DD were taken from the recent XLZD white paper [10]. Note that the proposed DARWIN experiment was expected to have a sensitivity very similar to XLZD (in its 40 ton baseline configuration), see the projected DARWIN limits in [45]. For the indirect detection bounds we use H.E.S.S. data from [16, 17], while the future projections for CTA were taken from refs. [18, 19].

All figures in this section show the numerical results in the plane Wilson coefficient, C_i , versus dark matter mass, m_{T^0} . As in fig. 4, we always set $\Lambda = 15$ TeV and $\lambda_{HT} = 0$. The region that reproduces correctly the relic density, as determined by PLANCK [4], is shown by a solid black band. The grey area to the right and below the black band indicates the excluded parameter regions with an overabundant dark matter density. Direct detection constraints and prospects are shown as dash-dotted (LZ) or dotted (XLZD) lines respectively, while indirect detection limits and prospects are marked with dashed lines. The most dominant channels for indirect detection were considered for each operator in the construction of the limits. These channels are indicated in the label of each plot as a subscript under the experiment name. In the figures, regions shown to the left or above the limit curves are either excluded by current direct or indirect detection experiments,⁸ or are projected to be within experimental sensitivity for the case of future experiments. Additionally, for figures 4 (right) and 8 (left), for clarity we have shaded the excluded (or within future experimental sensitivity) areas, as the exclusion regions are more complex.

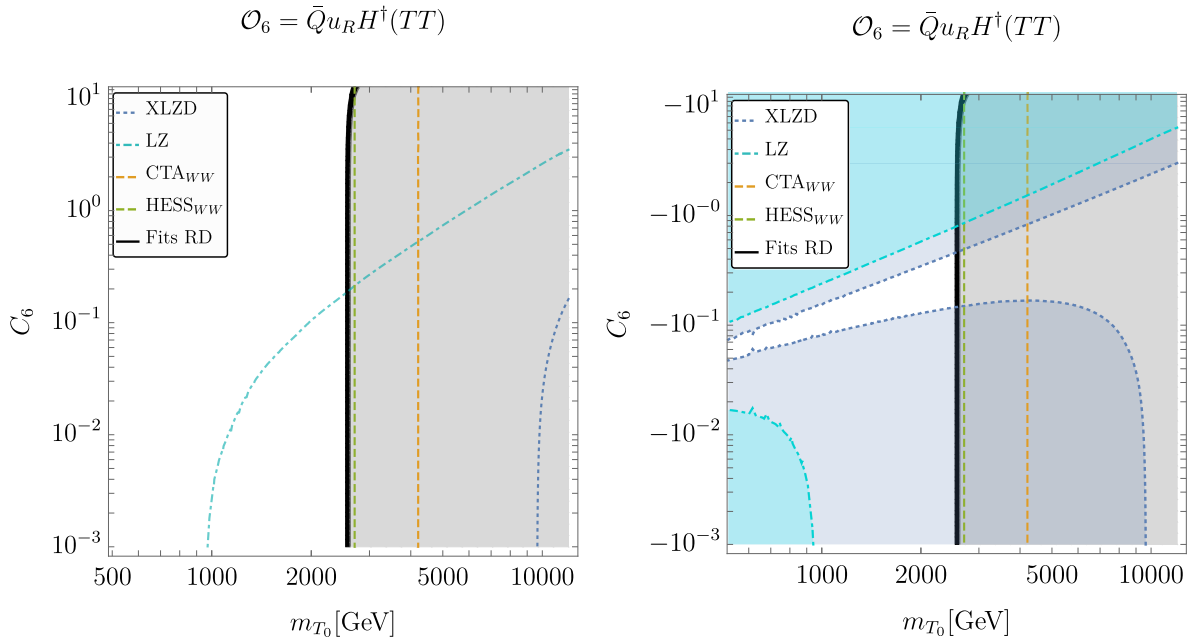


Figure 4: Operator \mathcal{O}_6 : Relic abundance, direct detection and indirect detection bounds and prospects in the Wilson coefficient vs. DM mass plane. **Left:** For positive values of the Wilson coefficient. **Right:** For negative values of the Wilson coefficient.

Let us discuss now the individual results in turn. We start with \mathcal{O}_6 , our example fermionic operator. Fig. 4 shows two plots for \mathcal{O}_6 , to the left the case of $C_6 > 0$, to the right $C_6 < 0$. As expected, the mass region which fits correctly the relic density is independent of the operator, except for C_6 very close to the non-perturbative limit, where a slight increase in mass is seen. Since this is the same for all fermionic operators, here we show only results for

⁸Note that some regions with masses below 500 GeV could be allowed by some specific experiment since both, direct and indirect detection bounds get weaker for small masses. However, this mass range is not relevant for us since it does not reproduce the observed relic abundance and is therefore not shown in the plots.

\mathcal{O}_6 . For effective operators involving quarks, the direct detection cross section is dominated by operators involving light quarks, while DM annihilation (indirect detection) is dominated by heavy-quark operators. In fig. 4, we consider the sum over all three generations of quarks for all flavor-conserving Wilson coefficients.

As the figure shows, ID constraints from H.E.S.S. already significantly constrain the model. Taken at face value, W^+W^- data seem to exclude the mass region with the correct relic density. However, recall that the constraints from H.E.S.S. use the Einasto profile and as the collaboration states in [16] other profiles could weaken the limits by up to two orders of magnitude. The future CTA experiment will improve sensitivity and very likely, provide a decisive test for \mathcal{O}_6 .

Also DD constraints rule out part of the available parameter space already. Here, however, the discussion depends on the sign of the Wilson coefficient. Consider first the case $C_6 > 0$. Here, existing DD constraints from LZ already rule out large values of C_6 in the mass region, which correctly fits the relic density. XLZD will test all the mass region that fits the relic density. For $C_6 < 0$ the situation is more complicated. Note that here we have coloured the region excluded (or to be tested) by LZ (XLZD), for an easier comprehension of the constraints: The white region in the middle of the plot will be left unconstrained even after XLZD. The rather strange shape of the DD constraint for $C_6 < 0$ can be traced back to a cancellation between the operator and the gauge contributions to the DD cross section.

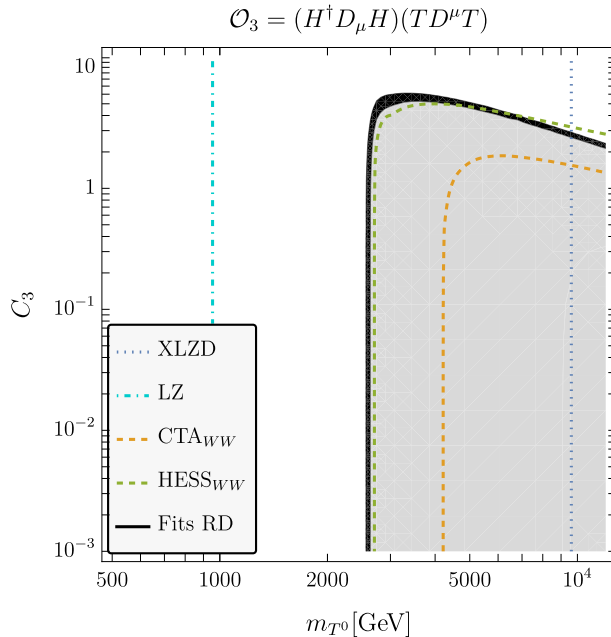


Figure 5: Operator \mathcal{O}_3 : Relic abundance, direct detection bounds, and indirect detection bounds in the Wilson coefficient vs. DM mass plane. For the indirect detection bounds (CTA_{WW} and $HESS_{WW}$) we have included both W^+W^- and ZZ annihilation modes since both are relevant for this operator and have similar gamma-ray spectra.

Fig. 5 shows the results for operator \mathcal{O}_3 . Here, we show only one plot, because results for positive and negative Wilson coefficients are identical. For large values of C_3 there is a new solution for explaining the correct relic density that extends to quite large dark matter

masses. In fact, we cut the plot at $m_{T^0} = 15$ TeV, since $m_{T^0} \geq \Lambda$ is not allowed in an EFT calculation, but solutions to fitting Ωh^2 exist for even larger masses (and larger values of Λ).

DD constraints on this operator are currently rather weak, but XLZD will probe masses up to $m_{T^0} \approx 9.5$ TeV in the future. H.E.S.S. results formally rule out the low-mass region again, but allow $m_{T^0} \geq 7$ TeV even for the optimistic Einasto profile. CTA will probe all mass regions, for which Ωh^2 can be correctly fitted, at least for the more favorable dark matter profiles.

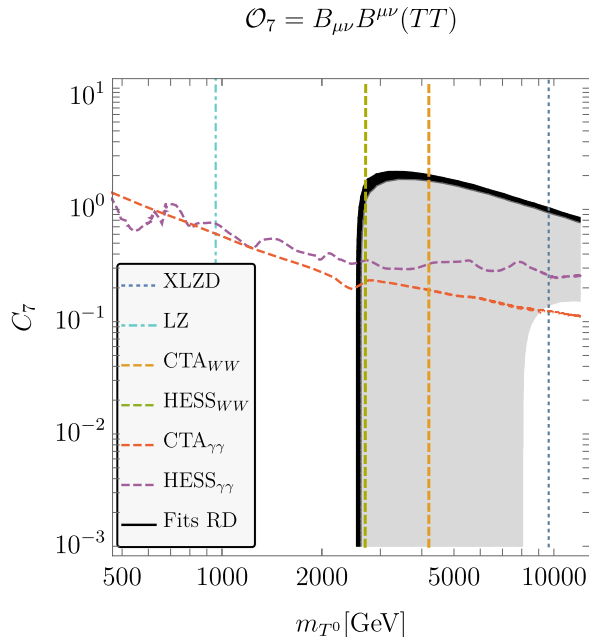


Figure 6: Operator \mathcal{O}_7 : Relic abundance, direct detection bounds, and indirect detection bounds in the Wilson coefficient vs. DM mass plane.

Results for \mathcal{O}_7 are shown in fig. 6. Results are independent of the sign of C_7 , as in the case of \mathcal{O}_3 , and also the parameter space for fitting the relic density is similar to the one discussed above for \mathcal{O}_3 . The main difference between \mathcal{O}_7 and \mathcal{O}_3 is that \mathcal{O}_7 is also constrained by searches of gamma-ray lines (HESS $_{\gamma\gamma}$ in the figure), which excludes the region where the operator has an impact on the relic abundance ($C_7 \gtrsim 7 \times 10^{-1}$). Considering, additionally, the bounds from HESS $_{WW}$, for this operator the whole region that fits the relic abundance is excluded by indirect detection (for the case of the Einasto profile). Thus, for \mathcal{O}_7 a sizeable contribution of the operator to DM phenomenology is already now disfavoured.

All the figures so far discussed include the effect of Sommerfeld enhancement on the relic abundance and indirect detection bounds. In fig. 7, upper panel, we show for illustration purposes both results, with and without Sommerfeld effect, for the case $C_8 > 0$. Note that, the calculation of the Sommerfeld enhancement for our specific case of scalar triplet DM with zero hypercharge, was done in ref. [21], from where we extracted the enhancement factor. The plot in the bottom panel of fig. 7 shows the case $C_8 < 0$. Note that constraints from H.E.S.S. again allow only particular mass and C_8 ranges (for the Einasto profile). We can see that for positive Wilson coefficients, there is a region that fits the relic density and is consistent with current constraints for relatively low DM masses ($1.7 \text{ TeV} \lesssim m_{T^0} \lesssim 2.5 \text{ TeV}$

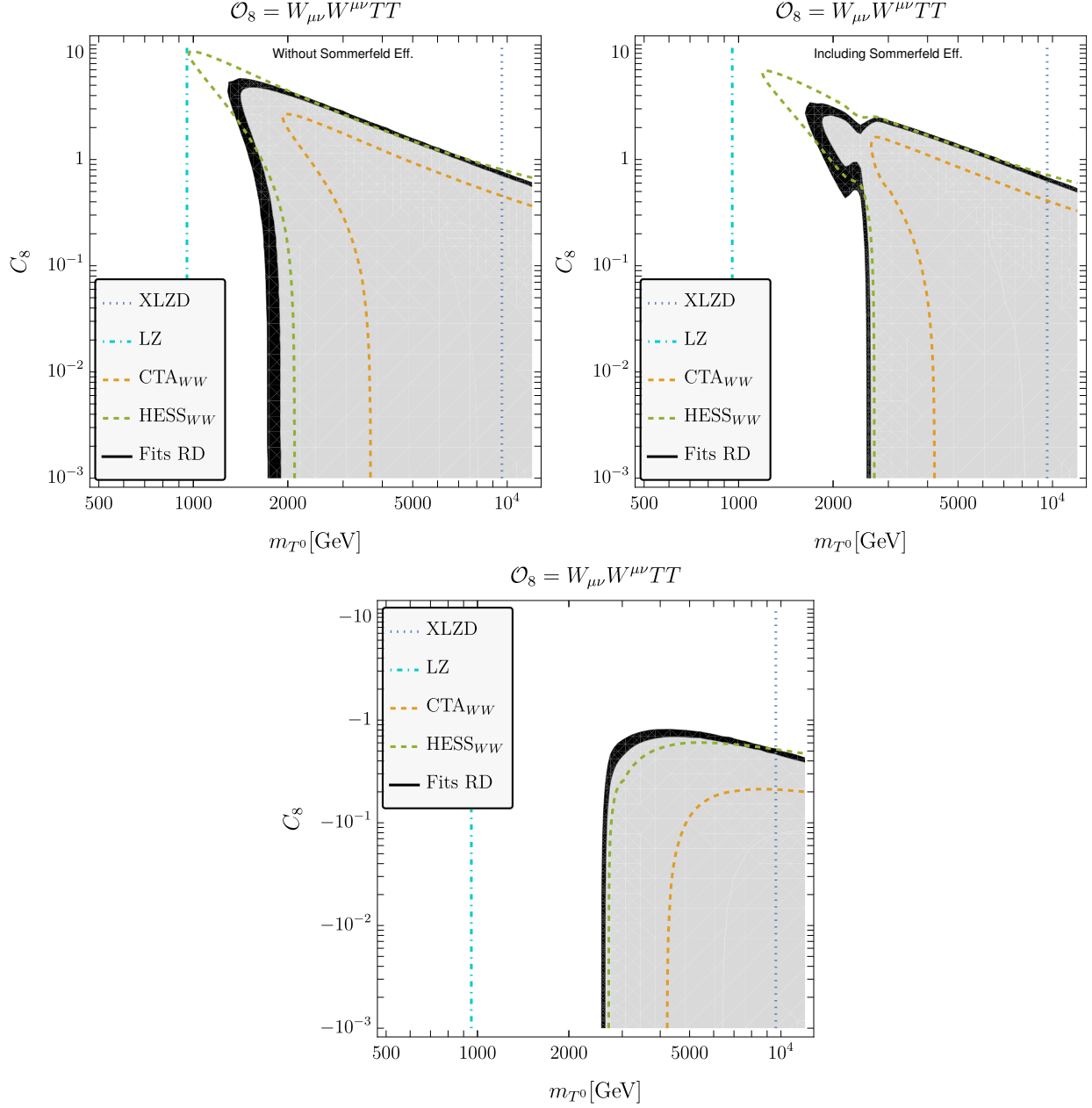


Figure 7: Operator \mathcal{O}_8 : Relic abundance, direct detection bounds, and indirect detection bounds in the Wilson coefficient vs. DM mass plane. For the indirect detection bounds (CTA_{WW} and $HESS_{WW}$) we have included both W^+W^- and ZZ annihilation modes since both are relevant in different mass ranges and have similar gamma-ray spectra (ZZ becomes important when the contribution of the operator interferes destructively with the pure gauge interactions.) **Upper left:** Without Sommerfeld effect. **Upper right:** Including Sommerfeld effect. **Bottom:** For negative values of the Wilson coefficient.

and $2 \lesssim C_8 \lesssim 4$). This region is allowed due to interference of this operator with pure gauge interactions and is not present for negative values of the Wilson coefficient (as can be seen in the bottom panel in fig. 7). Note also that large values of $m_{T^0} \gtrsim 8$ TeV remain allowed

for both signs of C_8 .

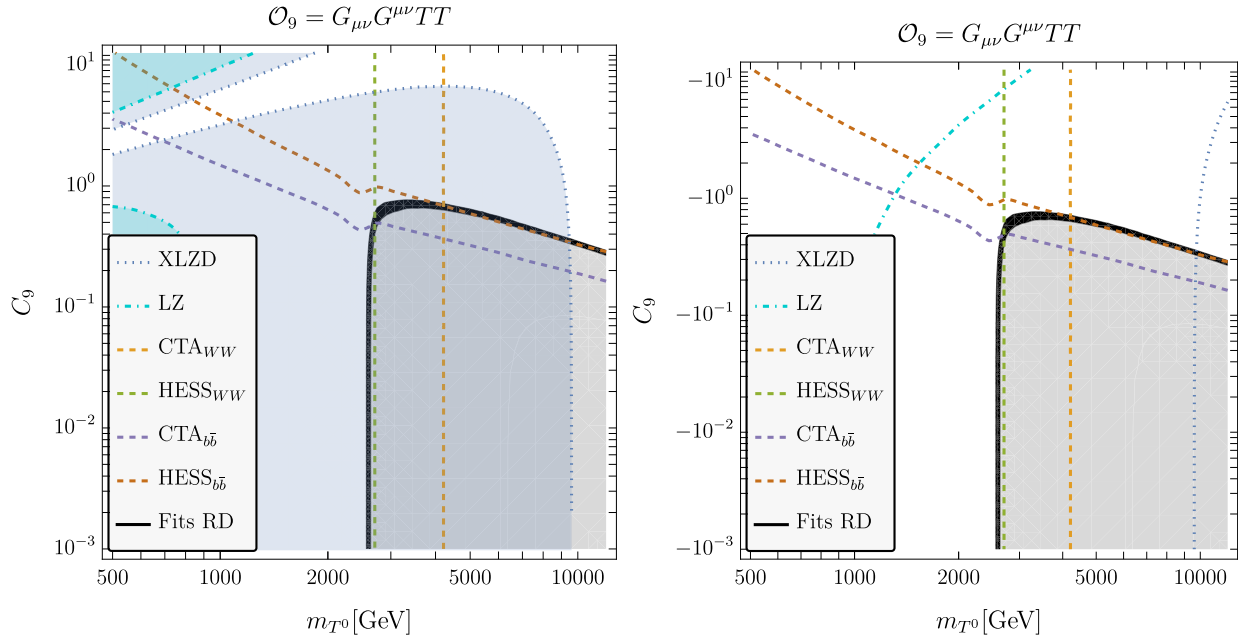


Figure 8: Operator \mathcal{O}_9 : Relic abundance, direct detection bounds, and indirect detection bounds in the Wilson coefficient vs. DM mass plane. **Left:** For positive values of the Wilson coefficient. Note that for both XLZD and LZ experiments here are two curves. The allowed region in each case corresponds to the area between these two curves. **Right:** For negative values of the Wilson coefficient.

Finally, for \mathcal{O}_9 , fig. 8, we can see that the region $2.6 \text{ TeV} \lesssim m_{T^0} \lesssim 3.5 \text{ TeV}$ (with $C_9 \approx \pm 7 \times 10^{-1}$) is consistent with the observed relic density and current constraints. This region will be probed in the future by CTA and XLZD experiments. Annihilation into pairs of u or d quarks yields a gamma-ray spectrum similar to that of annihilation into gluon pairs, while $c\bar{c}$ resembles $s\bar{s}$, and ZZ is analogous to W^-W^+ [46]. For this reason, and just to give an example, in fig. 8, we show also indirect detection limits from $\text{CTA}_{b\bar{b}}$ and $\text{HESS}_{b\bar{b}}$, because the gamma-ray spectrum of the $b\bar{b}$ channel is similar to $g\bar{g}$ [46], which is one of the dominant channels in this case.

In summary, in this section we have discussed the impact of a set of NRO $d = 6$ operators on the relic density of T^0 , as well as the direct and indirect detection constraints on these operators. Future indirect detection searches by CTA will provide an important test for these operators.

6 Conclusions

In this work we explored an extension of the standard model with a scalar triplet dark matter candidate within an effective field theory, which we denote as TSMEFT, i.e. the “standard model effective field theory supplemented by a scalar triplet”. We analyzed the effect of non-renormalizable dimension-6 operators on the DM relic abundance, the constraints on

the parameter space from both direct and indirect detection bounds and the prospects of testing the model with future experiments.

The inclusion of $d = 6$ operators can significantly affect the DM phenomenology compared to the minimal model where only the renormalizable interactions for scalar triplet are included [20, 21]. $d = 6$ operators can be classified into two groups: (i) purely bosonic operators and (ii) operators with fermions. For the bosonic operators we find that the relic density of the triplet can be changed drastically. Since for these operators the DM annihilation cross section is proportional to $\sigma \sim m_{T^0}^2/\Lambda^4$, the operators can completely dominate the relic density calculation at large values of m_{T^0} . This allows to reproduce the experimental value of Ωh_{DM}^2 for values of m_{T^0} in excess of 10 TeV, compared to $m_{T^0} \sim 2$ TeV (2.8 TeV) without (including) the Sommerfeld effect in the case of the renormalizable model. In contrast, operators involving fermions are chirally suppressed, i.e $\sigma \sim m_f^2$, and thus contribute only subdominantly to the total annihilation cross section, when compared with the gauge interactions. Fermionic operators therefore are mostly irrelevant for fixing the relic density of the triplet.

Our main results are summarized in figures 5-8. These figures show the viable parameter space in the plane DM mass vs Wilson coefficient, C_i , for the different operators. The plots show the parameter combinations that reproduce the observed relic abundance and add contours for current and future experimental constraints from direct (LZ [6], XLZD [10]) and indirect detection (H.E.S.S [16, 17], CTA [18, 19]) experiments. All the figures include the Sommerfeld effect for the relic abundance and the indirect detection bounds.

Current DD bounds from LZ do not yet constrain the parameter space, where the relic density is correctly fitted, with the exception of \mathcal{O}_6 , for which LZ data provides a significant upper limit on C_6 already. XLZD⁹, on the other hand, will provide lower limits on m_{T^0} of the order of nearly $\mathcal{O}(10)$ TeV, thus either ruling out large junk of the allowed parameter space or – formulated more optimistically - find dark matter, if TSMEFT is indeed the correct model.

In contrast, indirect detection provides some important constraints on the model already with current data. Searches by H.E.S.S in the W^+W^- , ZZ and $b\bar{b}$ channels [16] are on the verge of ruling out the pure renormalizable triplet model for masses that fit Ωh^2 correctly. Depending on the operator under consideration, H.E.S.S allows still to fit Ωh^2 correctly for several operators, but mostly for larger triplet masses. The improvements expected in the not-so-distant future from CTA data, however, especially when combining W^+W^-/ZZ and $\gamma\gamma$ channels, should lead to either a discovery of a DM signal or would rule out TSMEFT as the correct explanation for dark matter.

Let us add a disclaimer. We need to stress again, that we have taken both, the current ID data and the predictions for future experiments, at face value. Our optimistic conclusions depend strongly on the assumption that the astrophysics (in particular the assumed dark matter profiles) that went into the derivation of these limits are correct. Nevertheless, we think TSMEFT is an attractive dark matter model, since – different from many other proposals – it should be possible to either discover DM signals or rule out the model completely in the next decade or so.

⁹DARWIN is very similar to XLZD.

Name	Operator	# real parameters	+h.c.?
\mathcal{O}_{WBT}	$W^{\mu\nu}B_{\mu\nu}T$	1	no
\mathcal{O}_{LeHT}	$\bar{L}e_RHT$	18	yes
\mathcal{O}_{QdHT}	$\bar{Q}d_RHT$	18	yes
\mathcal{O}_{QuHT}	$\bar{Q}u_RH^\dagger T$	18	yes
\mathcal{O}_{H^4T}	$H^\dagger H^\dagger HHT$	1	no
$\mathcal{O}_{H^2T^3}$	$H^\dagger H TTT$	1	no
$\mathcal{O}_{L^2H^2T}$	$LLHHT$	18	yes

Table 2: Operators odd in T in TSMEFT. All operators in this table are $d = 5$, except the last one which is $d = 6$. These operators need to be eliminated, if T is to be a good DM candidate.

Acknowledgements

We would like to thank Alexander Pukhov for useful discussions about **MicrOMEGAs**. M.H. acknowledges support by Spanish grants PID2023-147306NB-I00 and CEX2023-001292-S (MCIU/AEI/10.13039/501100011033), as well as CIPROM/2021/054 (Generalitat Valenciana) and the MultiDark network, RED2022-134411-T. N.N. acknowledges support from ANID (Chile) FONDECYT Iniciación Grant No. 11230879. C.A. is supported by ANID-Chile FONDECYT grant No. 1231248 and ANID-Chile PIA/APOYO AFB230003. D.R. acknowledges support by Sostenibilidad UdeA, UdeA/CODI Grants 2022-52380 and 2023-59130, Minciencias Grants CD 82315 CT ICETEX 2021-1080. M.G acknowledges support from Centro de Física Teórica de Valparaíso (CeFiTeV) and project PFE UVA22991/PUENTE.

A Appendix

A.1 T -odd operators

In this appendix we give for completeness also the operators that are odd in T up to $d = 6$. All operators are given in table 2. As in table 1, we specify the fields involved in the operator and give the parameter counting, without spelling out the generation indices explicitly. If any of these operators is present in the theory, T will be unstable.

A.2 Operators for complex T

In this appendix we discuss for completeness also operators up to $d = 6$ that are non-zero only if T is assumed to be a complex field. Since T has hypercharge zero, it can be a self-conjugate

field. We work with this assumption throughout the paper.

However, one could also assume that T is complex and for that case more Lagrangian terms are allowed. For example, there are two types of mass terms for a complex T :

$$m_C^2 |T|^2 + \frac{1}{2} m_R^2 (T^2 + \text{h.c.}) \quad (15)$$

Similarly, for the non-renormalizable operators for complex T there are many more independent contractions. For example, the single T^6 will become 4 different terms: T^6 , $T^\dagger T^5$, $(T^\dagger)^2 T^4$ and $(T^\dagger)^3 T^3$. Most of the time, these new operators do not play any significant role for the dark matter phenomenology of T , but there are three possible exceptions:

$$\mathcal{O}_{e^2 T^2} = (\bar{e}_R \gamma_\mu e_R)(T^\dagger D^\mu T), \quad \mathcal{O}_{d^2 T^2} = (\bar{d}_R \gamma_\mu d_R)(T^\dagger D^\mu T), \quad \mathcal{O}_{u^2 T^2} = (\bar{u}_R \gamma_\mu u_R)(T^\dagger D^\mu T). \quad (16)$$

These operators, vanishing for real T , do have a non-zero effect on the relic density similar to $\mathcal{O}_{L^2 T^2}$ and $\mathcal{O}_{Q^2 T^2}$, that we discuss in the main text.

A.3 Tree-level UV completions for TSMEFT operators

In this appendix we give the tree-level decomposition for $d = 6$ TSMEFT operators with even number of T . From the 9 operators studied in detail in this paper only the first six operators given in table 1 can be decomposed at tree-level. The remaining three operators, $\mathcal{O}_7 - \mathcal{O}_9$, can be decomposed only at 1-loop.

Table 3 gives the decompositions for $\mathcal{O}_1 - \mathcal{O}_3$. These operators can be decomposed adding only one additional BSM field. The table indicates whether the internal field in the diagram is a vector (V) or fermion (F) and the transformation properties under the SM gauge group. Also, depending on the decomposition the internal particle needs to be either odd or even under a Z_2 , this is given as -1 or 1 in the last index of the field.

Name	Operator	Fields
\mathcal{O}_1	$(\bar{L} \gamma_\mu L)(T D^\mu T)$	$V_{1,1,0,1}, V_{1,3,0,1}, F_{1,2,1/2,-1}, F_{1,4,1/2,-1}$
\mathcal{O}_2	$(\bar{Q} \gamma_\mu Q)(T D^\mu T)$	$V_{1,1,0,1}, V_{1,3,0,1}, F_{3,2,1/6,-1}, F_{3,4,1/6,-1}$
\mathcal{O}_3	$(H^\dagger D_\mu H)(T D^\mu T)$	$S_{1,1,0,1}, S_{1,3,0,1}, S_{1,2,1/2,-1}, S_{1,4,1/2,-1},$ $V_{1,1,0,1}, V_{1,3,0,1}, V_{1,2,1/2,-1}, V_{1,4,1/2,-1}$

Table 3: Tree-level decompositions for operators even in T in TSMEFT at $d = 6$. Fields are given with their transformation properties under $SU(3)_c \times SU(2)_L \times U(1)_Y \times Z_2$. The last index indicates even or odd under Z_2 . This table gives operators that can be decomposed with one BSM field.

Table 4 gives the decompositions for operators $\mathcal{O}_4 - \mathcal{O}_6$. As can be seen from fig. 9, there are four possible diagrams for these ‘‘Yukawa-like’’ operators and all except the last diagram need two BSM fields to generate the operator.

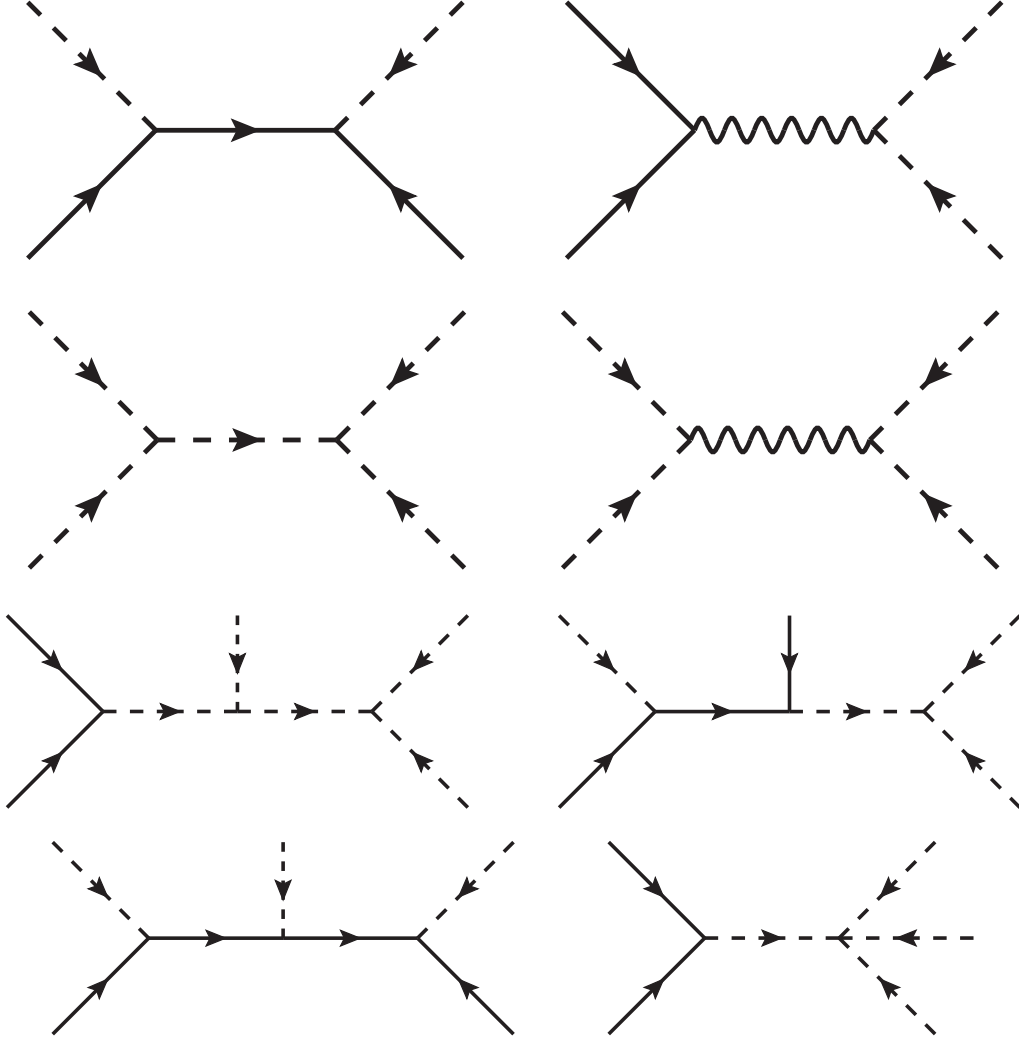


Figure 9: Diagrams for the decomposition of operators $\mathcal{O}_1 - \mathcal{O}_6$. Top line: $\mathcal{O}_{1,2}$; 2nd line: \mathcal{O}_3 . The bottom two lines are for $\mathcal{O}_4 - \mathcal{O}_6$. Here, three diagrams need two different BSM fields.

References

- [1] G. Bertone, D. Hooper and J. Silk, *Particle dark matter: Evidence, candidates and constraints*, *Phys. Rept.* **405** (2005) 279 [[hep-ph/0404175](#)].
- [2] G. Arcadi, M. Dutra, P. Ghosh, M. Lindner, Y. Mambrini, M. Pierre et al., *The waning of the WIMP? A review of models, searches, and constraints*, *Eur. Phys. J. C* **78** (2018) 203 [[1703.07364](#)].
- [3] L. Roszkowski, E.M. Sessolo and S. Trojanowski, *WIMP dark matter candidates and searches—current status and future prospects*, *Rept. Prog. Phys.* **81** (2018) 066201 [[1707.06277](#)].

Name	Operator	Fields
\mathcal{O}_4	$\bar{L}e_R H T T$	$(S_{1,2,1/2,1}, S_{1,2,1/2,-1}), (S_{1,2,1/2,1}, S_{1,4,1/2,-1}), (S_{1,2,1/2,1}, S_{1,1,0,1}), (S_{1,2,1/2,1}, S_{1,3,0,1}),$ $(F_{1,2,1/2,1}, F_{1,2,1/2,-1}), (F_{1,2,1/2,1}, F_{1,4,1/2,-1}), (F_{1,3,1,-1}, F_{1,1,1,1}), (F_{1,3,1,-1}, F_{1,3,1,1}),$ $(F_{1,3,1,-1}, F_{1,2,1/2,-1}), (F_{1,3,1,-1}, F_{1,4,1/2,-1}), (F_{1,2,1/2,1}, S_{1,1,0,1}), (F_{1,2,1/2,1}, S_{1,3,0,1}),$ $(F_{1,3,1,-1}, S_{1,2,1/2,-1}), (F_{1,3,1,-1}, S_{1,4,1/2,-1}), (F_{1,1,1,1}, S_{1,1,0,1}), (F_{1,3,1,1}, S_{1,3,0,1}),$ $(F_{1,2,1/2,-1}, S_{1,2,1/2,-1}), (F_{1,4,1/2,-1}, S_{1,4,1/2,-1}), S_{1,2,1/2,1}$
\mathcal{O}_5	$\bar{Q}d_R H T T$	$(S_{1,2,1/2,1}, S_{1,2,1/2,-1}), (S_{1,2,1/2,1}, S_{1,4,1/2,-1}), (S_{1,2,1/2,1}, S_{1,1,0,1}), (S_{1,2,1/2,1}, S_{1,3,0,1}),$ $(F_{3,2,1/6,1}, F_{3,2,1/6,-1}), (F_{3,2,1/6,1}, F_{3,4,1/6,-1}), (F_{3,3,1/3,-1}, F_{3,1,1/3,1}), (F_{3,3,1/3,-1}, F_{3,3,1/3,1}),$ $(F_{3,3,1/3,-1}, F_{3,2,1/6,-1}), (F_{3,3,1/3,-1}, F_{3,4,1/6,-1}), (F_{3,2,1/6,1}, S_{1,1,0,1}), (F_{3,2,1/6,1}, S_{1,3,0,1}),$ $(F_{3,3,1/3,-1}, S_{1,2,1/2,-1}), (F_{3,3,1/3,-1}, S_{1,4,1/2,-1}), (F_{3,1,1/3,1}, S_{1,1,0,1}), (F_{3,3,1/3,1}, S_{1,3,0,1}),$ $(F_{3,2,1/6,-1}, S_{1,2,1/2,-1}), (F_{3,4,1/6,-1}, S_{1,4,1/2,-1}), S_{1,2,1/2,1}$
\mathcal{O}_6	$\bar{Q}u_R H^+ T T$	$(S_{1,2,1/2,1}, S_{1,2,1/2,-1}), (S_{1,2,1/2,1}, S_{1,4,1/2,-1}), (S_{1,2,1/2,1}, S_{1,1,0,1}), (S_{1,2,1/2,1}, S_{1,3,0,1}),$ $(F_{3,2,1/6,1}, F_{3,2,1/6,-1}), (F_{3,2,1/6,1}, F_{3,4,1/6,-1}), (F_{3,3,2/3,-1}, F_{3,1,2/3,1}), (F_{3,3,2/3,-1}, F_{3,3,2/3,1}),$ $(F_{3,3,2/3,-1}, F_{3,2,1/6,-1}), (F_{3,3,2/3,-1}, F_{3,4,1/6,-1}), (F_{3,1,2/3,1}, S_{1,1,0,1}), (F_{3,1,2/3,1}, S_{1,3,0,1}),$ $(F_{3,2,1/6,-1}, S_{1,2,1/2,-1}), (F_{3,2,1/6,-1}, S_{1,4,1/2,-1}), (F_{3,2,1/6,1}, S_{1,1,0,1}), (F_{3,4,1/6,1}, S_{1,3,0,1}),$ $(F_{3,3,2/3,-1}, S_{1,2,1/2,-1}), (F_{3,3,2/3,-1}, S_{1,4,1/2,-1}), S_{1,2,1/2,1}$

Table 4: Tree-level decompositions for operators even in T in TSMEFT at $d = 6$: Yukawa-like operators. This table gives operators that need two BSM fields, except for the last decomposition corresponding to diagram in the bottom right of fig. 9.

- [4] PLANCK collaboration, *Planck 2018 results. VI. Cosmological parameters*, *Astron. Astrophys.* **641** (2020) A6 [[1807.06209](#)].
- [5] LZ collaboration, *First Dark Matter Search Results from the LUX-ZEPLIN (LZ) Experiment*, *Phys. Rev. Lett.* **131** (2023) 041002 [[2207.03764](#)].
- [6] LZ COLLABORATION collaboration, *Dark Matter Search Results from 4.2 Tonne-Years of Exposure of the LUX-ZEPLIN (LZ) Experiment*, [2410.17036](#).
- [7] XENON collaboration, *First Dark Matter Search with Nuclear Recoils from the XENONnT Experiment*, *Phys. Rev. Lett.* **131** (2023) 041003 [[2303.14729](#)].
- [8] DARWIN collaboration, *DARWIN: towards the ultimate dark matter detector*, *JCAP* **11** (2016) 017 [[1606.07001](#)].
- [9] J. Aalbers et al., *A next-generation liquid xenon observatory for dark matter and neutrino physics*, *J. Phys. G* **50** (2023) 013001 [[2203.02309](#)].

- [10] XLZD collaboration, *The XLZD Design Book: Towards the Next-Generation Liquid Xenon Observatory for Dark Matter and Neutrino Physics*, [2410.17137](#).
- [11] PANDAX collaboration, *PandaX-xT: a Multi-ten-tonne Liquid Xenon Observatory at the China Jinping Underground Laboratory*, [2402.03596](#).
- [12] S. Bottaro, D. Buttazzo, M. Costa, R. Franceschini, P. Panci, D. Redigolo et al., *Closing the window on WIMP Dark Matter*, *Eur. Phys. J. C* **82** (2022) 31 [[2107.09688](#)].
- [13] S. Bottaro, D. Buttazzo, M. Costa, R. Franceschini, P. Panci, D. Redigolo et al., *The last Complex WIMPs standing*, [2205.04486](#).
- [14] M. Cirelli, A. Strumia and J. Zupan, *Dark Matter*, [2406.01705](#).
- [15] H. Beauchesne and C.-W. Chiang, *Indirect detection constraints on semi-annihilation of inert scalar multiplets*, [2407.01096](#).
- [16] H.E.S.S. collaboration, *Search for Dark Matter Annihilation Signals in the H.E.S.S. Inner Galaxy Survey*, *Phys. Rev. Lett.* **129** (2022) 111101 [[2207.10471](#)].
- [17] H.E.S.S. collaboration, *Search for dark matter gamma-ray line annihilation signals in the H.E.S.S. Inner Galaxy Survey*, *PoS ICRC2023* (2023) 1424.
- [18] CTA collaboration, *Sensitivity of the Cherenkov Telescope Array to a dark matter signal from the Galactic centre*, *JCAP* **01** (2021) 057 [[2007.16129](#)].
- [19] CTAO collaboration, *Dark matter line searches with the Cherenkov Telescope Array*, *JCAP* **07** (2024) 047 [[2403.04857](#)].
- [20] M. Cirelli, N. Fornengo and A. Strumia, *Minimal dark matter*, *Nucl. Phys. B* **753** (2006) 178 [[hep-ph/0512090](#)].
- [21] M. Cirelli, A. Strumia and M. Tamburini, *Cosmology and Astrophysics of Minimal Dark Matter*, *Nucl. Phys. B* **787** (2007) 152 [[0706.4071](#)].
- [22] L. Lopez Honorez, E. Nezri, J.F. Oliver and M.H.G. Tytgat, *The Inert Doublet Model: An Archetype for Dark Matter*, *JCAP* **02** (2007) 028 [[hep-ph/0612275](#)].
- [23] F. Bishara, J. Brod, B. Grinstein and J. Zupan, *From quarks to nucleons in dark matter direct detection*, *JHEP* **11** (2017) 059 [[1707.06998](#)].
- [24] J. Brod, A. Gootjes-Dreesbach, M. Tamaro and J. Zupan, *Effective Field Theory for Dark Matter Direct Detection up to Dimension Seven*, *JHEP* **10** (2018) 065 [[1710.10218](#)].
- [25] J.C. Criado, A. Djouadi, M. Perez-Victoria and J. Santiago, *A complete effective field theory for dark matter*, *JHEP* **07** (2021) 081 [[2104.14443](#)].

- [26] L. Coito, C. Faubel, J. Herrero-García, A. Santamaria and A. Titov, *Sterile neutrino portals to Majorana dark matter: effective operators and UV completions*, *JHEP* **08** (2022) 085 [[2203.01946](#)].
- [27] J. Aebischer, W. Altmannshofer, E.E. Jenkins and A.V. Manohar, *Dark matter effective field theory and an application to vector dark matter*, *JHEP* **06** (2022) 086 [[2202.06968](#)].
- [28] J.-H. Liang, Y. Liao, X.-D. Ma and H.-L. Wang, *Dark sector effective field theory*, *JHEP* **12** (2023) 172 [[2309.12166](#)].
- [29] A. Pukhov, *CalcHEP 2.3: MSSM, structure functions, event generation, batches, and generation of matrix elements for other packages*, [hep-ph/0412191](#).
- [30] A. Alloul, N.D. Christensen, C. Degrande, C. Duhr and B. Fuks, *FeynRules 2.0 - A complete toolbox for tree-level phenomenology*, *Comput. Phys. Commun.* **185** (2014) 2250 [[1310.1921](#)].
- [31] G. Belanger, F. Boudjema, A. Pukhov and A. Semenov, *micrOMEGAs_3: A program for calculating dark matter observables*, *Comput. Phys. Commun.* **185** (2014) 960 [[1305.0237](#)].
- [32] G. Bélanger, F. Boudjema, A. Goudelis, A. Pukhov and B. Zaldivar, *micrOMEGAs5.0 : Freeze-in*, *Comput. Phys. Commun.* **231** (2018) 173 [[1801.03509](#)].
- [33] G. Belanger, A. Mjallal and A. Pukhov, *Recasting direct detection limits within micrOMEGAs and implication for non-standard Dark Matter scenarios*, *Eur. Phys. J. C* **81** (2021) 239 [[2003.08621](#)].
- [34] K. Griest and D. Seckel, *Three exceptions in the calculation of relic abundances*, *Phys. Rev. D* **43** (1991) 3191.
- [35] A. Belyaev, N.D. Christensen and A. Pukhov, *CalcHEP 3.4 for collider physics within and beyond the Standard Model*, *Comput. Phys. Commun.* **184** (2013) 1729 [[1207.6082](#)].
- [36] T. Katayose, S. Matsumoto, S. Shirai and Y. Watanabe, *Thermal real scalar triplet dark matter*, *JHEP* **09** (2021) 044 [[2105.07650](#)].
- [37] P. Bandyopadhyay, S. Parashar, C. Sen and J. Song, *Probing Inert Triplet Model at a multi-TeV muon collider via vector boson fusion with forward muon tagging*, *JHEP* **07** (2024) 253 [[2401.02697](#)].
- [38] W. Chao, G.-J. Ding, X.-G. He and M. Ramsey-Musolf, *Scalar Electroweak Multiplet Dark Matter*, *JHEP* **08** (2019) 058 [[1812.07829](#)].
- [39] J. Hisano, K. Ishiwata and N. Nagata, *Gluon contribution to the dark matter direct detection*, *Phys. Rev. D* **82** (2010) 115007 [[1007.2601](#)].

- [40] J. Hisano, K. Ishiwata and N. Nagata, *QCD Effects on Direct Detection of Wino Dark Matter*, *JHEP* **06** (2015) 097 [[1504.00915](#)].
- [41] J. Einasto, *On the construction of a composite model for the galaxy and on the determination of the system of galactic parameters*, *Trudy Astrofizicheskogo Instituta Alma-Ata, Vol. 5, p. 87-100, 1965* **5** (1965) 87.
- [42] J.F. Navarro, C.S. Frenk and S.D.M. White, *The Structure of cold dark matter halos*, *Astrophys. J.* **462** (1996) 563 [[astro-ph/9508025](#)].
- [43] J.F. Navarro, C.S. Frenk and S.D.M. White, *A Universal density profile from hierarchical clustering*, *Astrophys. J.* **490** (1997) 493 [[astro-ph/9611107](#)].
- [44] W. Atwood, A.A. Abdo, M. Ackermann, W. Althouse, B. Anderson, M. Axelsson et al., *The large area telescope on the fermi gamma-ray space telescope mission*, *The Astrophysical Journal* **697** (2009) 1071.
- [45] M. Schumann, L. Baudis, L. Büttikofer, A. Kish and M. Selvi, *Dark matter sensitivity of multi-ton liquid xenon detectors*, *JCAP* **10** (2015) 016 [[1506.08309](#)].
- [46] FERMI-LAT collaboration, *Sensitivity Projections for Dark Matter Searches with the Fermi Large Area Telescope*, *Phys. Rept.* **636** (2016) 1 [[1605.02016](#)].